Switchable all inorganic halide perovskite nanocrystalline photoelectrodes for solar-driven organic transformations

Roser Fernández-Climent,[1] Andrés F. Gualdrón-Reyes,[1,2] Miguel García-Tecedor,[‡] Camilo A. Mesa,[1] Drialys Cárdenas-Morcoso,[1,†] Laura Montañes,[1] Eva M. Barea,[1] Elena Mas-Marzá,[1] Beatriz Julián-López,[1] Iván Mora-Seró,[1,*] Sixto Giménez[1,*]

[1] Institute of Advanced Materials (INAM), Universitat Jaume I, Avenida de Vicent Sos Baynat, s/n, 12006 Castelló de la Plana, Spain

[2] Facultad de Ciencias, Instituto de Ciencias Químicas, Isla Teja, Universidad Austral de Chile, 5090000, Valdivia, Chile.

[‡] Present Address: Photoactivated Processes Unit, IMDEA Energy Institute, Parque Tecnológico de Móstoles, Avda. Ramón de la Sagra 3, 28935 Móstoles, Madrid, Spain.

[†] Present Address: Luxembourg Institute of Science and Technology, Materials Research and Technology Department, 41 Rue du Brill, L-4422, Belvaux, Luxembourg

Corresponding authors: sero@uji.es, sjulia@uji.es

Abstract

All inorganic halide perovskite nanocrystals (NCs) are considered fascinating materials for a wide range of optoelectronic applications encompassing photovoltaics, lasing, sensing and photocatalysis due to their outstanding optoelectronic properties. In the present study, we demonstrate that the photoelectrochemical behaviour of $CsPbBr_3$ NC films can be tailored through engineering the selective contacts and accepting species in the electrolyte. We have successfully applied this concept to the photoelectrochemical oxidation of benzyl alcohol (BzOH) to benzyl aldehyde (BzCHO) and the reverse photoelectrochemical reduction of BzCHO to BzOH, demonstrating that $CsPbBr_3$ NCs activate both reactions with photocurrents up to 40 $\mu A \cdot cm^{-2}$ towards BzCHO production and 5 $\mu A \cdot cm^{-2}$ for the reverse reaction at o.15 V vs NHE. The obtained results highlight the huge potential and versatility of halide perovskite NCs for photoelectrocatalytic applications, validating the implementation of these materials for a wide range of solar-driven complex organic transformations, and emphasizing the urgent need for

stabilization strategies to move beyond the proof-of-concept stage to relevant technological developments.

TOC
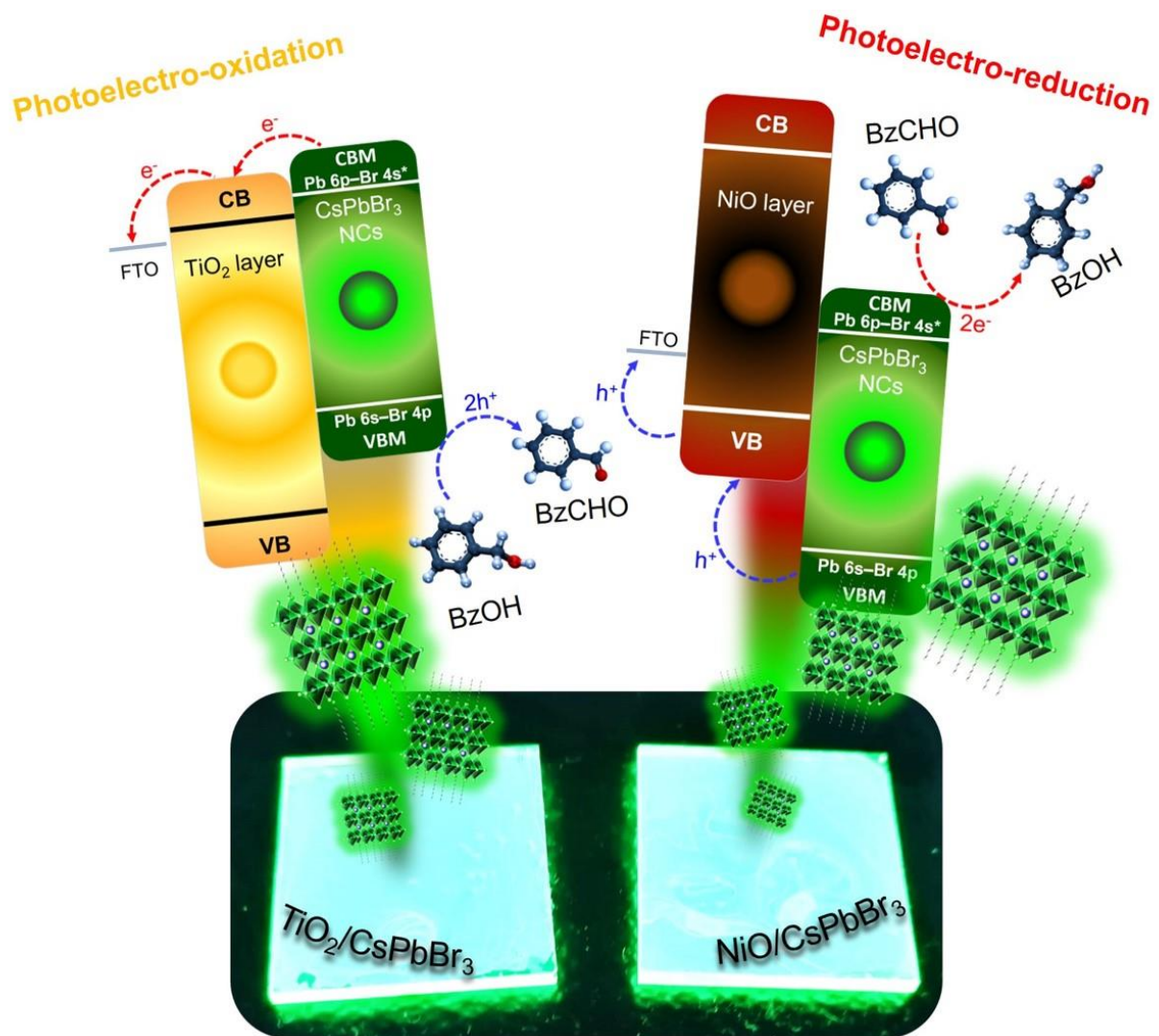
1. Introduction

All inorganic halide perovskite nanocrystals (NCs) have emerged in the last years as fascinating materials featuring defect-tolerant structure, high extinction coefficient,[1] ultrahigh photoluminescence quantum yield (PLQY),[2] multiple exciton generation, tunable bandgap (E_g) through composition engineering or quantum confinement effect,[3] as well as relatively high stability,[4] and good transport properties, resulting in long electron lifetimes.[5] These excellent optoelectronic properties have been successfully harnessed leading to breakthroughs in relevant solid-state energy conversion devices, such as photovoltaic solar cells,[6] light-emitting diodes (LEDs),[7] optically pumped lasers,[8] and photodetectors.[9] This broad range of optoelectronic applications takes advantage of the high PLQY of halide perovskite NCs due to their low non-radiative carrier recombination.[2b] More recently, these properties have also triggered the interest of these systems for solar-driven photocatalysis,[10] since the solar energy harvested and stored in excited photocarriers can be used to drive chemical reactions. Indeed, the exploration of photocatalytic and photoelectrochemical applications with inorganic halide perovskite NCs is receiving increasing attention,[10-11] due to their proven ability to transfer photogenerated charges to a liquid solution targeting: H_2 generation,[12] degradation of dyes and organic pollutants,[13] organic transformations[3b, 14], CO_2 reduction,[15] C-C coupling,[16] and photoelectrochemical sensing.[11a]

Most of these studies focused on photocatalytic applications, given the higher functional compatibility of the as-synthesized colloidal NCs with photocatalysis. In contrast, photoelectrochemical (PEC) applications require the homogeneous deposition of the colloidal NCs on (semi)conductive substrates, challenging the overall functional and mechanical stability of the films. However, the inherent advantages of the PEC configuration promoting the photoinduced charge separation and increasing the redox potential toward high productivity, have prompted researchers to circumvent the existing experimental and interpretation limitations, setting boundary conditions and protocols for (photo)electrochemical experiments with these materials.[17] In the present study, we demonstrate that the photoelectrochemical behavior of these materials can be tailored by the adequate selection of selective contacts (e.g. hole and electron transporting layers) and accepting species in the electrolyte. This interfacial engineering approach has already been successfully applied to other state-of-the-art photoactive materials like PbS nanocrystals,[18]

organic bulk heterojunctions[19] and photoactive MOFs,[20] prompting the wide applicability of these materials for novel PEC domains. Here, we have targeted the organic transformation of benzyl alcohol (BzOH) to benzyl aldehyde (BzCHO, photoelectro-oxidation) and the reverse reaction (photoelectro-reduction) as a proof-of-concept to validate the versatility of these materials for more sustainable synthetic pathways and energy conversion schemes, including both oxidation and reduction reactions that can be tailored at will. Indeed, the current industrial synthesis of BzCHO involves stoichiometric oxidation by toxic and hazardous dichromate and permanganate salts, or by liquid phase chlorination and oxidation of toluene. Consequently, the addressed photoelectrochemical method is expected to provide a highly selective and more sustainable process in concordance with the principles of Green Chemistry.[21] In this context, the photocatalytic oxidation of BzOH has already been addressed with organic-inorganic hybrid halide perovskite NCs,[14] showing the promising activity and selectivity of halide perovskites towards organic transformations. In the present study, we move a step forward, demonstrating that selective contact engineering provides a simple design tool for tailored photoelectrochemical behavior of these fascinating materials, which could in a subsequent step be utilized for more complex energy conversion schemes.

2. Results and discussion

CsPbBr$_3$ NCs prepared by hot-injection exhibited the expected cubic morphology, (**Figure 1**a), with an average size of ∼10 nm (**Figure 1**b) and featuring a bright green emission (508 nm) under UV illumination (**Figure 1**c). The NCs were spin-coated on FTO/TiO$_2$ and FTO/NiO substrates obtaining continuous and homogeneous films on both substrates as observed by AFM images, see **Figure 1**d and **1**g, respectively, and **Supporting Information, Figure S1** for SEM top views. The homogeneous CsPbBr$_3$ NC thin films exhibited ∼60 nm thickness on both substrates, TiO$_2$ and NiO, as evidenced by the cross-section SEM images in **Figure 1**e and **1**h, respectively. Their crystalline structure, identified through XRD, is shown as **Figure 1**f and **1**i, for NC layers deposited on TiO$_2$ and NiO substrates, respectively. Representative peaks are associated with the (100), (110), (200), (210), (211) and (202) planes from the perovskite structure with a cubic phase (JCPDS card # 00-054-0752), consistently with previous studies.[22] The underlying TiO$_2$ and NiO layers are also clearly identified on top of the 350 nm thick FTO layers from the cross-section images featuring thicknesses of approximately 30-40 nm, see Supporting Information, **Figure S2**

and S3. Their chemical composition, qualitatively estimated through EDS analyses, is shown as **Supporting Information, Figure S2** and **Table S1** and their crystalline structure identified from XRD measurements (anatase TiO_2, and cubic NiO, although a small fraction of NiO_x is also identified for this material) is detailed in **Supporting Information, Figure S4**. Steady-state photoluminescence (PL) measurements were also conducted on the NCs films deposited on glass, FTO, TiO_2 and NiO substrates, featuring an emission peak at 516 nm and a slight reduction of the Full-Width-at-Half-Maximum (FWHM) PL in the $FTO/TiO_2/NCs$ and FTO/NiO/NCs compared to the references glass/NCs and FTO/NCs. (**Supporting Information, Figure S5**a). This clearly indicates that the nature of the substrate does not modify the optical properties of the NCs, and provides particle size uniformity. On the other hand, the PL dynamics of the NCs was monitored by TRPL measurements (**Supporting Information, Figure S5**b). A slower PL decay was obtained in $FTO/TiO_2/NCs$ and FTO/NiO/NCs films, compared to the reference FTO/NCs film, while glass/NCs film exhibits the longest PL decay. By fitting the PL decays through a bi-exponential function, $y = y_0 + A_1 e^{-x/t1} + A_2 e^{-x/t2}$, their corresponding average electron lifetimes, τ_{avg}, were estimated as 18.5, 23.7, 21.4 and 25.7 ns from NCs deposited on FTO, FTO/TiO_2, FTO/NiO and glass, respectively **(Supporting Information Table S2)**. This is a clear evidence that the carrier transfer is promoted faster in FTO substrate, which does not present any selectivity to one type of photocarriers from NCs. However, the PL dynamics of $CsPbBr_3$ NCs is retarded when contacts such as TiO_2 and NiO layers are introduced. This feature is pivotal to facilitate the selective extraction of electrons or holes, respectively, and promote the photoelectrochemical oxidation and reduction of organic compounds, as shown below.
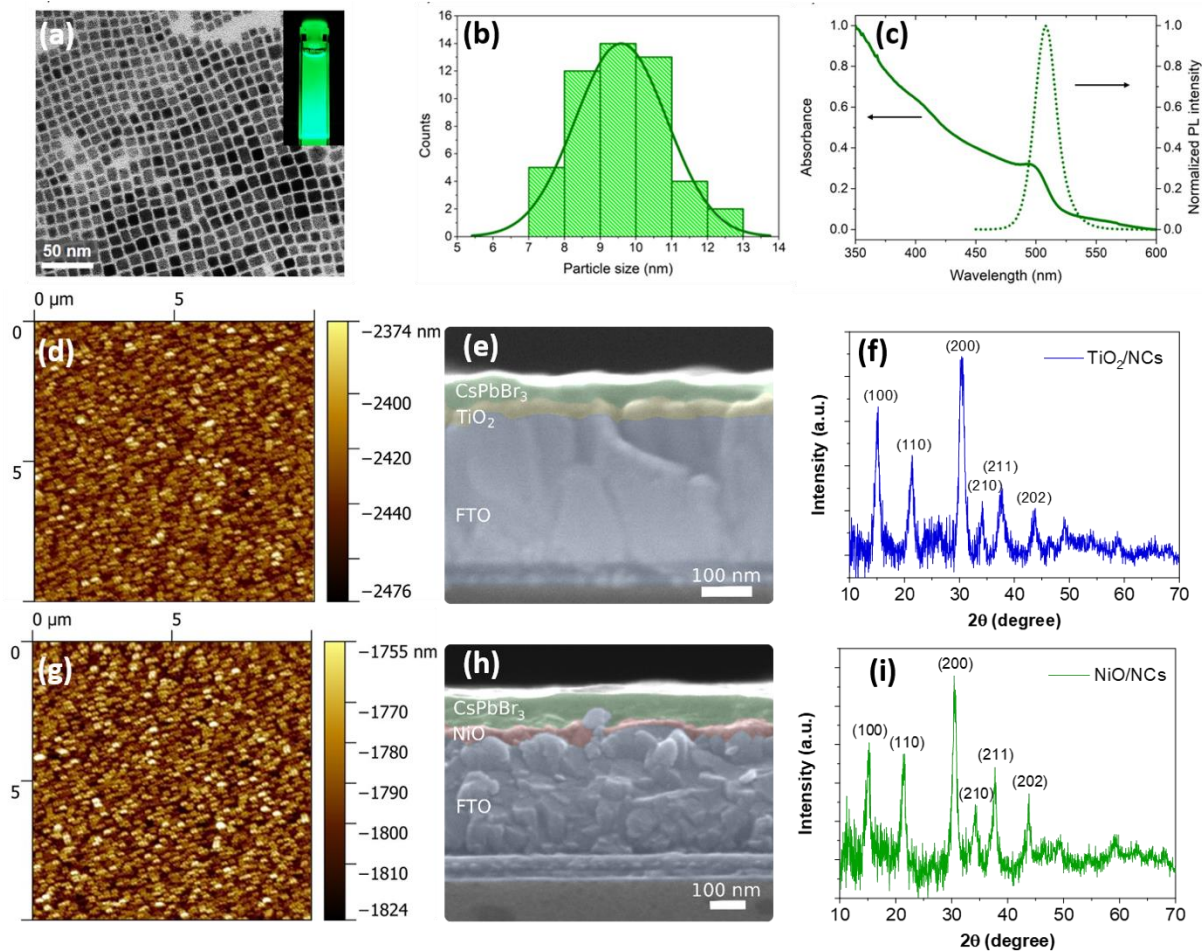
Figure 1.- (a) Representative TEM image, (b) size distribution and (c) optical absorbance and emission spectra of the as-synthesized CsPbBr$_3$ NCs, (d) AFM top-view, (e) cross-section SEM images and (f) XRD diffractogram of the as-synthesized FTO/TiO$_2$/CsPbBr$_3$ heterostructured electrodes. (g) AFM top-view, (h) cross-section SEM images and (i) XRD diffractogram of the as-synthesized FTO/NiO/CsPbBr$_3$ heterostructured electrodes.

The optical absorptance of the TiO$_2$ and NiO films without and with the CsPbBr$_3$ NCs clearly shows their enhanced light harvesting efficiency upon deposition of the NCs (**Figure 2**a), extending the absorption range from 350 nm to 550 nm, in good agreement with their optical absorbance reported in **Figure 1**b. The photoelectrochemical behavior of the as-prepared films was evaluated in 0.1 M tetrabutylammonium hexafluorophosphate in dichloromethane according to previous studies,[17, 22b] which reported the optimized stability of the CsPbBr$_3$ NCs in these conditions. Cyclic voltammetry measurements in the dark and under illumination revealed the photoanodic behavior of FTO/TiO$_2$/CsPbBr$_3$ NCs electrodes, as showed in **Figure 2**b. In this

configuration, photogenerated holes at the halide perovskite NCs are driven towards the electrode/liquid solution interface, oxidizing the electron donor species, while the photogenerated electrons are driven to the TiO_2 contact and injected to the external circuit. These electrons lead to the reduction of the electron acceptor species at the cathode, closing the electronic circuit.

$$BzCHO \overset{+2\ H^+}{\underset{-2\ e^-}{\rightleftharpoons}} BzOH$$
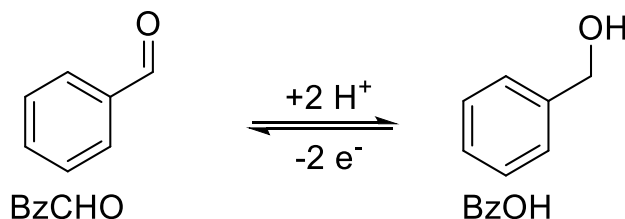
Scheme 1. Schematic of the reduction of benzaldehyde (BzCHO) and oxidation of benzyl alcohol (BzOH) reactions.

Blank measurements with and without the $CsPbBr_3$ NCs layer confirmed the contribution of the $CsPbBr_3$ NCs enhancing this anodic photocurrent, see **Supporting Information, Figure S6**a. Interestingly, the addition of BzOH (concentration 0.05 M) leads to a four-fold increase of this anodic photocurrent, reflecting the activity of $CsPbBr_3$ NCs to photoelectro-oxidize this organic substrate at the photoelectrode/electrolyte interface. On the other hand, cyclic voltammograms of the FTO/NiO/NCs films in the dark and under illumination confirmed the photocathodic behavior of these electrodes, driving the photogenerated electrons to the semiconductor/liquid interface and transferring them to electron acceptors in the solution. Upon addition of BzCHO as an electron acceptor, the photocurrent exhibits a three-fold enhancement, boosting from 50 $\mu A \cdot cm^{-2}$ to 150 $\mu A \cdot cm^{-2}$ (see **Figures 2**c and **S6**b), highlighting the favored photo-reduction ability of the electrode for this two-electron transformation (see **scheme 1**). The successful photoelectro-oxidation of BzOH to BzCHO and the reverse photoelectro-reduction reactions could be performed in a parallel tandem arrangement of photoanode and photocathode operating at 42 $\mu A \cdot cm^{-2}$ as shown in **Figure 2**d. This result, as a proof-of-concept, opens new horizons on solar-driven electrochemical applications with halide perovskite NCs, spanning from redox-flow batteries[23] to solar-driven fuel cells.[24]

Transformation of BzOH into BzCHO, through a two-hole reaction was analytically monitored by HPLC. The chromatograms after the respective reactions show an increase in intensity with respect

to the blank before the reaction at the retention times assigned to each product (1.28 min for benzyl alcohol and 1.57 min for benzaldehyde) as shown in Figure S7. Therefore, in view of these results, both conversions are confirmed to be taking place. We note here that the quantification of BzCHO as well as BzOH for both oxidation and reduction reactions, proved to be challenging due to the low product concentration given by the low achieved photocurrents and stabilities of our photoelectrodes, detaching after a few minutes of operation. Few attempts of BzOH oxidation with perovskite NCs are shown in literature, for example, Huang *et. al.*, reported the photocatalytic oxidation of BzOH with TiO_2/organic inorganic halide perovskite NCs with a 60 % conversion rate, in an 8 hours experiment illuminating with a Xe lamp (with a AM1.5G filter to simulate the solar spectrum).[14] Indeed, several hours are generally needed in photocatalytic/photoelectrochemical experiments for the reliable assessment of both productivity and selectivity.[25] For example, a recent study with metal oxide photoanodes ($BiVO_4$) operating at higher current densities, was conducted for more than 12 hours for a quantitative assessment.[26] It is also plausible that once the $CsPbBr_3$ NCs detach from the electrode, they continue working as photocatalysts, with the reduction of BzCHO to BzOH being thermodynamically favorable compared to the oxidation of BzOH. This is supported by the relative positions of the valence and conduction bands with the redox position of the BzCHO/BzOH couple (see **Figure 4** and further discussion in the **Supporting Information**). Optical photographs of the photoelectrodes before and after electrochemical testing, under visible and UV illumination are showed as Supporting Information, Figure S8.
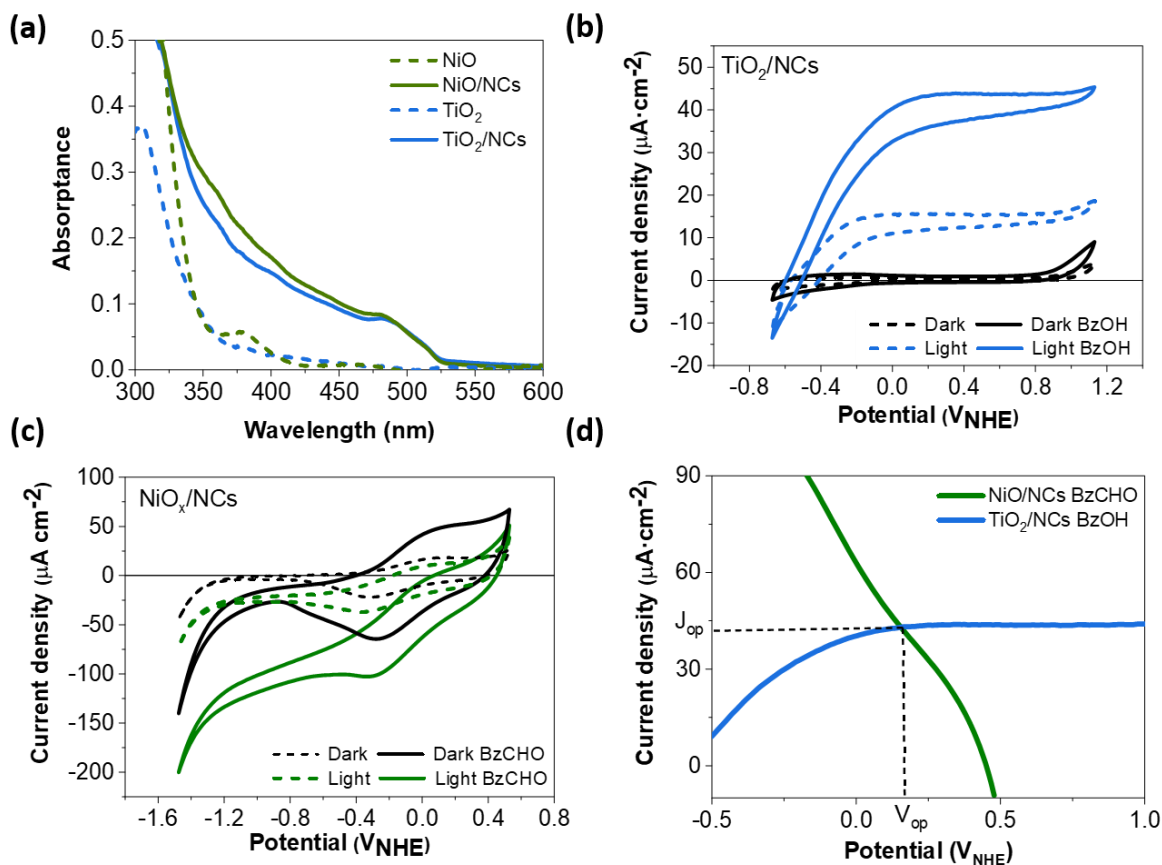
Figure 2.- (a) Optical absorbance of the FTO/TiO$_2$ and FTO/NiO photoanodes with and without CsPbBr$_3$ NCs, (b) Cyclic voltammetry curves in the dark and under illumination showing the photocurrents of FTO/TiO$_2$/CsPbBr$_3$ NCs photoanodes with and without BzOH substrate in 0.1 M Bu$_4$NPF$_6$ in dichloromethane electrolyte, (c) Cyclic voltammetry curves in the dark and under illumination showing the photocurrents of FTO/NiO/CsPbBr$_3$ NCs photocathodes with and without BzCHO substrate in 0.1 M Bu$_4$NPF$_6$ in dichloromethane electrolyte, (d) Operation condition of the tandem arrangement of a photoanode and a photocathode for a photo-assisted BzOH/BzCHO fuel cell. A 400 nm high pass neutral filter was used to suppress photoexcitation of TiO$_2$ and NiO selective contacts or a plausible formation of singlet oxygen under UV light, which could react with the organic species.[26]

Further insights into carrier dynamics were obtained through exploring the dependence of both photocurrent (J$_{ph}$) and photovoltage (V$_{ph}$) with illumination intensity. These parameters were measured for both photoanode and photocathode configurations, as illustrated in **Figure 3**. The photocurrent was evaluated at the working potential estimated from **Figure 2**d, (0.15 V vs. NHE)

and the photo-voltage is defined as $V_{ph} = V_{light} - V_{dark}$, where V_{dark} and V_{light} are the open circuit potentials in the dark and under illumination (with filtered light < 400 nm), respectively. Both the FTO/TiO$_2$/NCs photoanode and FTO/NiO/NCs photocathodes show a linear dependence of J$_{ph}$ with light intensity, see **Figure 3**a, **3**b, **3e** and **3f**, suggesting fast hole (electron) transfer kinetics from the CsPbBr$_3$ Valence (Conduction) Band to the BzOH (BzCHO), involving kinetic control of the photocurrent.[20] However, V$_{ph}$ does not show a monotonic trend with light intensity, particularly at low light intensities (see **Figure 3**c, **3**d for oxidation and **3g**, **3i** for reduction), which could be related to the existence of surface defects leading to Fermi level pinning.[27] On the other hand, we note that oxidation photocurrents (**Figure 3a**) decrease with time, while this is not the case for reduction photocurrents (**Figure 3e**), which we attribute to the significantly higher photocurrent values recorded for the oxidation tests.

The switchable photoelectrochemical (PEC) activity of the CsPbBr$_3$ NCS films towards oxidation and reduction reactions of BzOH and BzCHO, respectively can be rationalized through the energy diagrams scheduled in **Figure 4**. The relative positions of conduction and valence band of the heterostructured FTO/TiO$_2$/NCs and FTO/NiO/NCs electrodes were extracted from the literature.[22b, 28] From these energy diagrams, it is clear that both BzOH oxidation and BzCHO reduction are thermodynamically favorable with photogenerated carriers at CsPbBr$_3$ NCs in the developed heterostructured electrodes, consistently with the voltammograms showed in **Figure 2**. Indeed, higher thermodynamic driving force exists for the photoelectro-reduction of BzCHO, compared to the photoelectro-oxidation of BzOH, which may account for the enhanced photocurrents reported here for this reduction reaction. Consequently, interfacial engineering of all-inorganic halide perovskite NCs provides a versatile tool to harness the excellent optoelectronic properties of these materials towards sustainable photoelectrochemical transformations, highlighting the need for estabilization of these materials under operation conditions to move from proof-of-concept to more relevant technological developments. Promising on-going strategies, like ligand passivation[3b] or core/shell structures,[10] will be key to achieve this goal.
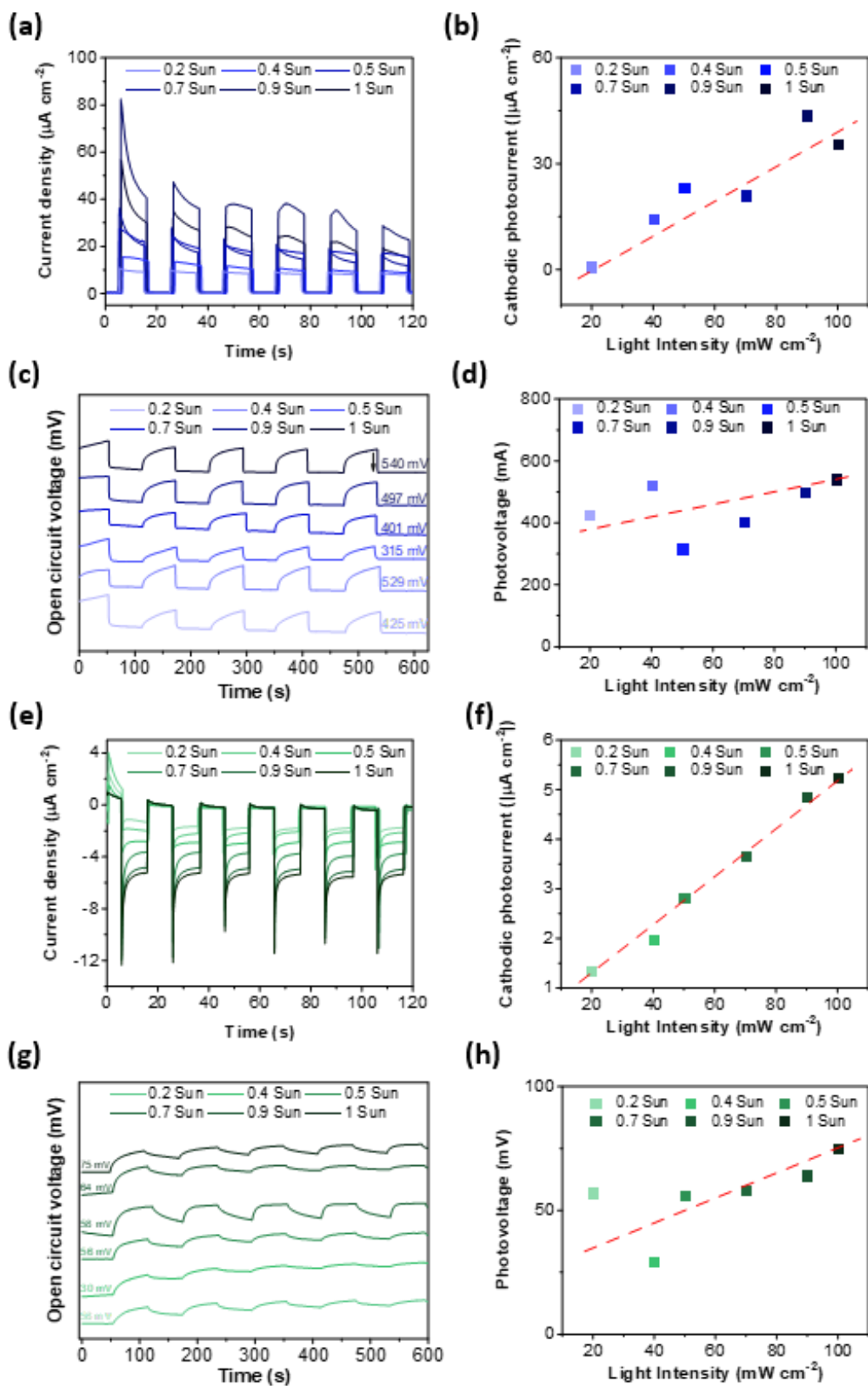
(a) Current density (μA cm⁻²) vs Time (s) — 0.2 Sun, 0.4 Sun, 0.5 Sun, 0.7 Sun, 0.9 Sun, 1 Sun

(b) Cathodic photocurrent (|μA cm⁻²|) vs Light Intensity (mW cm⁻²) — 0.2 Sun, 0.4 Sun, 0.5 Sun, 0.7 Sun, 0.9 Sun, 1 Sun

(c) Open circuit voltage (mV) vs Time (s) — 0.2 Sun, 0.4 Sun, 0.5 Sun, 0.7 Sun, 0.9 Sun, 1 Sun; 540 mV, 497 mV, 401 mV, 315 mV, 529 mV, 425 mV

(d) Photovoltage (mA) vs Light Intensity (mW cm⁻²) — 0.2 Sun, 0.4 Sun, 0.5 Sun, 0.7 Sun, 0.9 Sun, 1 Sun

(e) Current density (μA cm⁻²) vs Time (s) — 0.2 Sun, 0.4 Sun, 0.5 Sun, 0.7 Sun, 0.9 Sun, 1 Sun

(f) Cathodic photocurrent (|μA cm⁻²|) vs Light Intensity (mW cm⁻²) — 0.2 Sun, 0.4 Sun, 0.5 Sun, 0.7 Sun, 0.9 Sun, 1 Sun

(g) Open circuit voltage (mV) vs Time (s) — 0.2 Sun, 0.4 Sun, 0.5 Sun, 0.7 Sun, 0.9 Sun, 1 Sun; 75 mV, 64 mV, 58 mV, 56 mV, 30 mV, 56 mV

(h) Photovoltage (mV) vs Light Intensity (mW cm⁻²) — 0.2 Sun, 0.4 Sun, 0.5 Sun, 0.7 Sun, 0.9 Sun, 1 Sun

12

Figure 3.- (a) (e) Chronoamperometric and chronovoltammetric (c) (g) measurements at different illumination intensities for (a) (c) BzOH photo-oxidation, (e) (g) BzCHO photo-reduction. The values of photopotential are indicated numerically, next to the specific plot. Relevant photocurrents and photopotentials corresponding to Figures (a), (c), (e) and (g) are showed as (b), (d), (f) and (h), respectively. The red dashed lines serve as eye guides. All measurements were performed in 0.05 M BzOH (a) (c) or 0.05 M BzCHO (e) (g) in 0.1 M Bu$_4$NPF$_6$ in dichloromethane electrolyte.
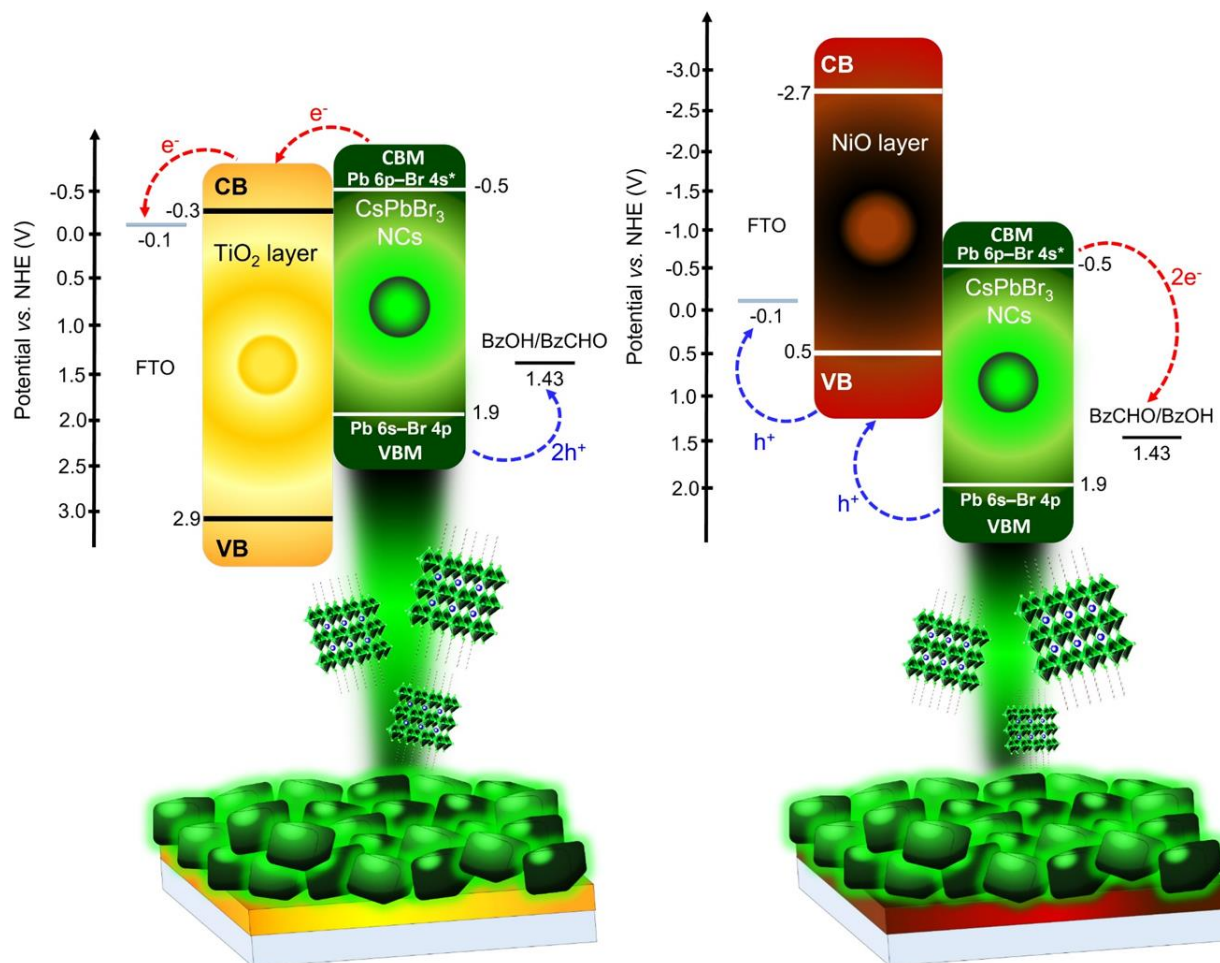

Figure 4.- Band diagram of the CsPbBr$_3$ and redox potential of the benzyl alcohol / benzaldehyde. The relative positions of conduction and valence band of the heterostructured FTO/TiO$_2$/NCs and FTO/NiO/NCs electrodes were extracted from the literature.[22b, 28]

3. Conclusions

We have demonstrated the switchable photoelectrochemical behavior of heterostructured $CsPbBr_3$ NCs films upon selective contact engineering and applied this concept to the solar-driven transformation of BzOH into BzCHO and vice versa. Meaningful photocurrents of 40 $\mu A \cdot cm^{-2}$ and 5 $\mu A \cdot cm^{-2}$ are obtained at 0.15 V vs NHE for photoelectro-oxidation and photoelectro-reduction reactions, respectively. Kinetic control of the photocurrent takes place for both two-carrier reactions and absence of surface states participating in the charge transfer mechanisms is evidenced for BzOH oxidation, while photovoltage saturation for the photocathodic reaction may indicate Fermi level pinning. The proposed energy diagram is consistent with the functional behavior reported and validates the strategy of selective contact engineering towards PEC applications with these materials. Further efforts are compulsory for the stabilization of NCs films under operation in a liquid solution, so the findings of the present study can translate into meaningful technological developments. Remarkably, the obtained results can pave the way towards a wide range of solar-driven Green Synthesis of organic compounds, as well as the application of these fascinating materials for advanced electrochemical applications like redox flow batteries and solar-driven fuel cells.

4. Experimental methods

Chemical and solvents: Nickel acetate tetrahydrate ($Ni(OAc)_2 \cdot 4H_2O$, 98% Alfa Aesar), 2-methoxyethanol (MeOEtOH, 99%, Fisher Chemical), and monoethanolamine (MEA, Sigma Aldrich), Nickel (II) acetylacetonate (95%, Sigma-Aldrich), Hydrochloric acid (37%, ACS reagent, Sigma-Aldrich), Dichloromethane HPLC grade (VWR Chemicals BDH), Tetrabutylammonium hexafluorophosphate (TBFP, 98%, Sigma-Aldrich), Cs_2CO_3 (99.9 %, Sigma-Aldrich), oleic acid (OA, 90 %, Sigma-Aldrich), 1-octadecene (1-ODE, 90 %, Sigma-Aldrich), $PbBr_2$ (ABCR, 99.998%), oleylamine (OLA, 98 %, Sigma-Aldrich), methyl acetate (MeOAc, 99.5%, Sigma Aldrich), hexane (CHROMASOLV, 99.7 %, Honeywell), n-octane (Alfa Aesar) were used as received from the chemical suppliers without further purification.

Synthesis of CsPbBr3 NCs: $CsPbBr_3$ perovskite NCs were obtained by a hot-injection synthetic protocol through stoichiometrically mixing both the Cs-oleate and $PbBr_2$ solutions as described elsewhere[3b, 22b] with some modifications. The corresponding chemicals were used without

purification processes. To obtain the Cs-oleate solution, Cs_2CO_3 (0.61 g, 1.87 mmol) and oleic acid (OA, 1.9 mL, 5.98 mmol) were mixed in 30 mL of 1 octadecene (1-ODE) into a 50 mL-three neck flask under vacuum for 30 min at 120 °C and kept under vacuum for 30 min. The mixture was heated to reach 150 °C under N_2-purge to dissolve the Cs_2CO_3 completely. In order to prevent the Cs-oleate precipitation to produce Cs_2O, the resultant solution was kept at 120 °C under vacuum.

In order to synthesize pure $CsPbBr_3$, $PbBr_2$ (0.85 g, 2.32 mmol) was mixed with 50 mL 1-ODE into a 100 mL-three neck flask and then degasified at 120 °C under vigorous stirring for 1 h. Then, 5 mL of each preheated OA (5 mL, 15.8 mmol) and oleylamine (5 mL, 15.2 mmol) were added to the flask at heated again at 170 °C. Simultaneously, 4 mL of preheated Cs-oleate was swiftly injected at this temperature into $PbBr_2$ solution, obtaining a green precipitate in the colloidal solution. Immediately, the flask was immersed into an ice bath for 5 s to quench the reaction. For isolating process, a two-steps purification of NCs was performed. First, the dispersed NCs were centrifuged at 5000 rpm for 5 min with methyl acetate (MeOAc) (all final NCs liquor washed with 120 mL MeOAc). The precipitated NCs were recovered from supernatant and re-dispersed in 5 mL of hexane. Second, 6 mL of MeOAc was added to the NCs dispersion and centrifuged again at 5000 rpm for 5 min. The NCs solid was separated from supernatant and redispersed with hexane. The final colloidal solution was stored in the fridge for at least 24 h before use, in order to decant residual products. The colloidal NCs solution was dried in a N_2 atmosphere and the precipitate was concentrated at 50 mg/mL with octane for further analysis.

Synthesis of NiO precursor solution: 5 mL of NiO precursor solution was prepared by mixing 50 µL of 38% HCl and 5 mL anhydrous ethanol. Then, Nickel (II) acetylacetonate (129 mg, 0.5 mmol) was added to the mixture and the resulting solution was left stirring overnight at room temperature. Before using the solution, it was filtered to remove undissolved material. The solution was left to stand before filtering to allow sedimentation to occur, then the clear solution was taken from the top and filtered with Poly(tetrafluoroethylene) (PTFE hydrophobe, 0.22 µm particle size, Labbox).

Preparation of NiO/ $CsPbBr_3$ and TiO_2/ $CsPbBr_3$ films: First, 2.5 × 2.5 cm^2 FTO substrates (Pilkington, TEC-15) were washed with soap/Milli-Q water, then rinsed with ethanol and finally with a 3:1 isopropanol-acetone solution sonicating during 15 min each one and dried under air

flow. Before spin-coating the metal oxide layer, the substrates were treated under UV-O_3 for 15 min. To deposit the nickel oxide layer, the NiO precursor solution described above (70 μL) was spin-coated at 5000 rpm and 1200 ac for 30 s. Then, after drying on a hot plate at 100 °C during 1 min, the as-deposited NiO layer was annealed at 375 °C for 45 min. To deposit the TiO_2 layer, a Ti-alkoxide solution (ShareChem, SC-BT060, 80 μL) was spin-coated at 4000 rpm and 1000 ac for 30 s. The as-deposited TiO_2 layer was dried at 150 °C for 10 min. Then, the TiO_2 films were annealed at 500 °C for 30 min. Three layers of the purified $CsPbBr_3$ NCs solution in octane were deposited by spin-coating on either NiO or TiO_2 layer at 1000 rpm for 30 s. Between each $CsPbBr_3$ NCs layer deposition, the substrates were cleaned, first, using a solution composed by 10 mg mL^{-1} of $Pb(NO_3)_2$ in methyl acetate and dried under nitrogen flow and then with neat methyl acetate and dried again. The procedure to prepare the $Pb(NO_3)_2$/methyl acetate solution is reported elsewhere.[29]

Structural and optical characterization: XRD diffraction data was carried out with a D4 Endeavor system (Bruker-AXS) with Cuk$_\alpha$ radiation (λ= 1.5406 Å). The morphology of the different samples was analyzed with a JEOL JEM-3100 Field Emission Scanning Electron Microscope (FE-SEM) including EDS analysis. The topography of the samples was recorded using AFM atomic force microscope (Concept Scientific Instrument) on a relatively large area (10 x10 μm). The optical properties of the prepared colloidal solutions and films were determined using a Lambda 1050+ Perkin Elmer UV/Vis/IR spectrophotometer. The absorbance (A) of the thin films was estimated from transmittance (T) and diffuse reflectance (R) measurements using an integrating sphere as A = −log(T + R), and the absorptance (*a*) was calculated as $a = 1 - 10^{-A}$. Steady-state and time-resolved photoluminescence (PL) measurements were conducted through photoluminescence spectrophotometer (Fluorolog 3-11, Horiba). An excitation wavelength of 420 nm was used to perform the PL measurements. The wavelength range for the measurements was 450–600 nm. Time resolved PL measurements (TRPL) were carried out at 405 nm pulsed laser (NanoLED-405L, <100 ps of pulse width, 1 MHz frequency).

Photoelectrochemical characterization: Cyclic voltammetry, linear sweep voltammetry and chronoamperometric measurements were performed on a commercial H-cell (PECH H-cell 2x1.5 ml, RedoxMe) in three-electrode configuration, using an Autolab Potentiostat/ Galvanostat. A Nafion 212 (FuelCellStore) membrane was used to separate the anodic and cathodic

compartments. A non-aqueous Ag/AgNO$_3$ electrode (ALS, Japan) and a Platinum wire were used as reference and counter electrode, respectively. FTO/TiO$_2$/CsPbBr$_3$ and FTO /NiO/CsPbBr$_3$ electrodes were used as the working electrode on the oxidation and reduction reactions, respectively. A solution of 0.1 M Tetrabutylammonium hexafluorophosphate (Bu$_4$NPF$_6$) in dichloromethane was used as supporting electrolyte. 0.05 M BzOH/0.05 M BzCHO were the initial concentrations in the oxidation and reduction compartments, respectively. To calibrate the system to the Normal Hydrogen Electrode (NHE) scale, the Ferrocene/Ferrocenium (Fc/Fc$^+$) couple was used as internal standard, by adding 1.9 mM of ferrocene after the electrochemical tests. Films were back-side illuminated with a Xe lamp at 1 sun, filtering the UV light with a 400 nm high pass neutral filter to avoid the photoelectrocatalytic activity of both TiO$_2$ and NiO layers. Identification and quantification of evolved products was carried out by High-Performance Liquid Chromatography (HPLC) performed on a 1260 Infinity II Agilent equipment. An Agilent (poroshell EC-C18, 4.6x100 mm, 2.7µm) set at 40.0 ^{o}C and a DAD detector (UV range) column was used for product separation and detection. The eluent rate used was 0.9 mL/mL a 35%-65% water-acetonitrile mixture and the volume of sample injection was 5.0 µL. Faradaic efficiencies (%FE) were calculated according to the expression: $FE = \frac{n_{experimental}}{n_{theoretical}} \cdot 100$. The theoretical moles were calculated by the Faraday's law: $n_{theoretical} = \frac{j \cdot t}{n \cdot F}$, where j is the current density recorded during the chronoamperometry measurement, t is the time in seconds, n is the number of electrons transferred in the reaction (n=2 in the addressed reactions) and F is the Faraday constant, 96485.33 C mol^{-1}, $n_{experimental}$ was determined by HPLC.

Supporting Information

Supporting information is available free of charge at:

Acknowledgments

References

[1]   J. Maes, L. Balcaen, E. Drijvers, Q. Zhao, J. De Roo, A. Vantomme, F. Vanhaecke, P. Geiregat, Z. Hens, *The Journal of Physical Chemistry Letters* **2018**, 9, 3093.

[2]   a) L. Protesescu, S. Yakunin, M. I. Bodnarchuk, F. Krieg, R. Caputo, C. H. Hendon, R. X. Yang, A. Walsh, M. V. Kovalenko, *Nano Letters* **2015**, 15, 3692; b) A. F. Gualdron-Reyes, S. Masi, I. Mora-Sero, *Trends in Chemistry* **2021**, 3, 499.

[3]   a) M. Suri, A. Hazarika, B. W. Larson, Q. Zhao, M. Vallés-Pelarda, T. D. Siegler, M. K. Abney, A. J. Ferguson, B. A. Korgel, J. M. Luther, *ACS Energy Letters* **2019**, 4, 1954; b) A. F. Gualdron-Reyes, J. Rodriguez-Pereira, E. Amado-Gonzalez, J. Rueda-P, R. Ospina, S. Masi, S. J. Yoon, J. Tirado, F. Jaramillo, S. Agourani, V. Munoz-Sanjose, S. Gimenez, I. Mora-Sero, *Acs Applied Materials & Interfaces* **2020**, 12, 914.

[4]   Z. Shi, Y. Li, Y. Zhang, Y. Chen, X. Li, D. Wu, T. Xu, C. Shan, G. Du, *Nano Letters* **2017**, 17, 313.

[5]   S. Seth, T. Ahmed, A. De, A. Samanta, *ACS Energy Letters* **2019**, 4, 1610.

[6]   a) J. Yuan, A. Hazarika, Q. Zhao, X. Ling, T. Moot, W. Ma, J. M. Luther, *Joule* **2020**, 4, 1160; b) M. Hao, Y. Bai, S. Zeiske, L. Ren, J. Liu, Y. Yuan, N. Zarrabi, N. Cheng, M. Ghasemi, P. Chen, M. Lyu, D. He, J.-H. Yun, Y. Du, Y. Wang, S. Ding, A. Armin, P. Meredith, G. Liu, H.-M. Cheng, L. Wang, *Nature Energy* **2020**, 5, 79.

[7]   a) X. Zhang, C. Sun, Y. Zhang, H. Wu, C. Ji, Y. Chuai, P. Wang, S. Wen, C. Zhang, W. W. Yu, *The Journal of Physical Chemistry Letters* **2016**, 7, 4602; b) Y.-K. Wang, F. Yuan, Y. Dong, J.-Y. Li, A. Johnston, B. Chen, M. I. Saidaminov, C. Zhou, X. Zheng, Y. Hou, K. Bertens, H. Ebe, D. Ma, Z. Deng, S. Yuan, R. Chen, L. K. Sagar, J. Liu, J. Fan, P. Li, X. Li, Y. Gao, M.-K. Fung, Z.-H. Lu, O. M. Bakr, L.-S. Liao, E. H. Sargent, *Angewandte Chemie International Edition* **2021**, n/a.

[8]   Y. Wang, X. Li, J. Song, L. Xiao, H. Zeng, H. Sun, *Advanced Materials* **2015**, 27, 7101.

[9]   a) M. I. Saleem, S. Yang, R. Zhi, M. Sulaman, P. V. Chandrasekar, Y. Jiang, Y. Tang, A. Batool, B. Zou, *Advanced Materials Interfaces* **2020**, 7, 2000360; b) C. Bi, S. V. Kershaw, A. L. Rogach, J. Tian, *Advanced Functional Materials* **2019**, 29, 1902446.

[10]   H. Huang, B. Pradhan, J. Hofkens, M. B. J. Roeffaers, J. A. Steele, *ACS Energy Letters* **2020**, 5, 1107.

[11]   a) J. Liang, D. Chen, X. Yao, K. Zhang, F. Qu, L. Qin, Y. Huang, J. Li, *Small* **2020**, 16, 1903398; b) X.-D. Wang, N.-H. Miao, J.-F. Liao, W.-Q. Li, Y. Xie, J. Chen, Z.-M. Sun, H.-Y. Chen, D.-B. Kuang, *Nanoscale* **2019**, 11, 5180.

[12]   M. Xiao, M. Hao, M. Lyu, E. G. Moore, C. Zhang, B. Luo, J. Hou, J. Lipton-Duffin, L. Wang, *Advanced Functional Materials* **2019**, 29, 1905683.

[13]   a) G. Gao, Q. Xi, H. Zhou, Y. Zhao, C. Wu, L. Wang, P. Guo, J. Xu, *Nanoscale* **2017**, 9, 12032; b) D. Cardenas-Morcoso, A. F. Gualdrón-Reyes, A. B. Ferreira Vitoreti, M. García-Tecedor, S. J. Yoon, M. Solis de la Fuente, I. Mora-Seró, S. Gimenez, *The Journal of Physical Chemistry Letters* **2019**, 10, 630.

[14]   H. Huang, H. Yuan, K. P. F. Janssen, G. Solís-Fernández, Y. Wang, C. Y. X. Tan, D. Jonckheere, E. Debroye, J. Long, J. Hendrix, J. Hofkens, J. A. Steele, M. B. J. Roeffaers, *ACS Energy Letters* **2018**, 3, 755.

[15]   a) Y.-F. Xu, M.-Z. Yang, B.-X. Chen, X.-D. Wang, H.-Y. Chen, D.-B. Kuang, C.-Y. Su, *Journal of the American Chemical Society* **2017**, 139, 5660; b) M. Ou, W. G. Tu, S. M. Yin, W. N. Xing, S. Y. Wu, H. J. Wang, S. P. Wan, Q. Zhong, R. Xu, *Angewandte Chemie-International Edition* **2018**, 57, 13570.

[16]   K. Wang, H. Lu, X. Zhu, Y. Lin, M. C. Beard, Y. Yan, X. Chen, *ACS Energy Letters* **2020**, 5, 566.

[17]   G. F. Samu, R. A. Scheidt, P. V. Kamat, C. Janáky, *Chemistry of Materials* **2018**, 30, 561.

[18]   I. Mora-Sero, L. Bertoluzzi, V. Gonzalez-Pedro, S. Gimenez, F. Fabregat-Santiago, K. W. Kemp, E. H. Sargent, J. Bisquert, *Nature Communications* **2013**, 4.

[19]   A. Guerrero, M. Haro, S. Bellani, M. R. Antognazza, L. Meda, S. Gimenez, J. Bisquert, *Energy & Environmental Science* **2014**, 7, 3666.

[20]   R. Ifraemov, R. Shimoni, W. He, G. Peng, I. Hod, *Journal of Materials Chemistry A* **2019**, 7, 3046.

[21]   T. Mallat, A. Baiker, *Chemical Reviews* **2004**, 104, 3037.

[22]   a) A. B. F. Vitoreti, S. Agouram, M. Solis de la Fuente, V. Muñoz-Sanjosé, M. A. Schiavon, I. Mora-Seró, *The Journal of Physical Chemistry C* **2018**, 122, 14222; b) D. Cardenas-Morcoso, A. F. Gualdron-Reyes, A. B. F. Vitoreti, M. Garcia-Tecedor, S. J. Yoon, M. S. de la Fuente, I. Mora-Sero, S. Gimenez, *Journal of Physical Chemistry Letters* **2019**, 10, 630.

[23]   J. Azevedo, T. Seipp, J. Burfeind, C. Sousa, A. Bentien, J. P. Araújo, A. Mendes, *Nano Energy* **2016**, 22, 396.

[24]   D. Shapiro, J. Duffy, M. Kimble, M. Pien, *Solar Energy* **2005**, 79, 544.

[25]   R. Li, H. Kobayashi, J. Guo, J. Fan, *The Journal of Physical Chemistry C* **2011**, 115, 23408.

[26]   R. Arcas, E. Peris, E. Mas-Marzá, F. Fabregat-Santiago, *Sustainable Energy & Fuels* **2021**, 5, 956.

[27]   P. Salvador, M. G. Hidalgo, A. Zaban, J. Bisquert, *The Journal of Physical Chemistry B* **2005**, 109, 15915.

[28]   a) Q. A. Akkerman, M. Gandini, F. Di Stasio, P. Rastogi, F. Palazon, G. Bertoni, J. M. Ball, M. Prato, A. Petrozza, L. Manna, *Nature Energy* **2016**, 2, 16194; b) N. Subha, M. Mahalakshmi, M. Myilsamy, B. Neppolian, V. Murugesan, *Journal of Photochemistry and Photobiology A: Chemistry* **2019**, 379, 150.

[29]   E. M. Sanehira, A. R. Marshall, J. A. Christians, S. P. Harvey, P. N. Ciesielski, L. M. Wheeler, P. Schulz, L. Y. Lin, M. C. Beard, J. M. Luther, *Science Advances* **2017**, 3, eaao4204.